Applied Thermal Engineering 299 (2026) 131197

Contents lists available at ScienceDirect

Applied Thermal Engineering

journal homepage: www.elsevier.com/locate/apthermeng

Research Paper

Experimental analysis of a gyroid-based heat and mass exchanger for Maisotsenko cooling cycle

Nicolò Morselli [a,*], Salvatore Cristiano [a], Marco Puglia [a], Simone Pedrazzi [a,b], Giulio Allesina [a,b]

[a] Department of Engineering "Enzo Ferrari", University of Modena and Reggio Emilia, Via Vivarelli 10/1, 41125 Modena, Italy
[b] INTERMECH Inter-Departmental Center, University of Modena and Reggio Emilia, Via Vivarelli 10/1, 41125 Modena, Italy

A B S T R A C T

The increasing global demand for space cooling, driven primarily by climate change, highlights the need for sustainable alternatives to vapor-compression systems and dew-point evaporative cooling is emerging as a promising solution in this context, as it enables efficient air temperature reduction to levels lower than those achievable with conventional evaporative systems. This work presents a first experimental investigation of an innovative cross-flow heat and mass exchanger (HMX) based on gyroid triply periodic minimal surfaces applied to the Maisotsenko cycle, marking a shift from traditional parallel-plate paradigms by introducing a fundamentally different 3D heat and mass transfer topology that leverages complex geometric structures to enhance thermal performance.

The device, manufactured in polylactic acid (PLA) through material extrusion, is characterized by a hydraulic diameter of 9.16 mm and has been tested at inlet air temperatures of 30 °C and 35 °C, with corresponding relative humidities of 43% and 32%, air velocities from 2.3 to 4.1 m/s and recirculation rates between 0.2 and 0.7.

The HMX achieved a maximum temperature drop of 6.1 °C and a volumetric cooling capacity of 55.6 kW/m^3, exceeding the typical values reported in literature for standard geometries. The maximum coefficient of performance (COP) of 9.1 was obtained at 35 °C, with $r \approx 0.2$ and air velocity of ≈2.5 m/s.

The results indicate that the turbulence-promoting nature of the gyroid geometry shifts the optimal operating range toward significantly lower air velocities (<2.5 m/s) compared to conventional planar HMX configurations, while higher velocities (≈4 m/s) lead to a rapid degradation of COP. Although the wet-bulb effectiveness was limited to slightly above 50% by both the conductive thermal resistance of PLA and the relatively short length of the HMX, the gyroid structure sustained intense mass transfer, maintaining outlet relative humidity above 83%, indicating an oversized wet channel and motivating geometrically asymmetric designs with longer dry channels and wider wet channels.

1. Introduction

In recent decades, the global rise in ambient temperatures coupled with accelerated urban development has led to a substantial increase in the demand for air conditioning [1], which is now recognized as critical for maintaining indoor thermal comfort, safeguarding public health, and enhancing climate resilience. However, the widespread deployment of these systems has raised significant concerns regarding their environmental footprint and energy consumption. The predominant technology in the cooling sector is vapor compression refrigeration (VCR), which constitutes the majority of systems currently in operation worldwide. VCR systems are valued for their reliability and economic viability, yet they are also characterized by high electricity usage and reliance on refrigerants with considerable global warming potential. As the urgency surrounding energy efficiency and greenhouse gas mitigation intensifies, alternative cooling approaches are gaining attention [2].

One promising alternative is represented by evaporative cooling (EC) technologies, which represent a class of energy-efficient solutions which exploit the latent heat of water evaporation to reduce air temperature. These systems are generally categorized into direct evaporative coolers (DEC) and indirect evaporative coolers (IEC) [3]. In DEC, the supply air is cooled and humidified as it passes through a wet medium and this process can lower the dry-bulb temperature toward the wet-bulb limit, achieving wet-bulb effectiveness (ε_{wb}) within 70–95% range [4]. However, increased indoor humidity and health concerns, such as microbial growth, may limit its use in residential or commercial settings [5].

IEC separates cooling effect from humidification since air is split into two streams: the working air undergoes evaporation, while the product air is cooled via heat transfer with the working air without moisture gain. Although ideal conditions could allow the product air to reach the wet-bulb temperature, practical limitations such as imperfect counter-flow and limited heat transfer surfaces reduce ε_{wb} to 40–80% [6].

Compared to VCR systems, EC technologies offer several advantages: they rely exclusively on water as a natural refrigerant, they operate using 100% outdoor air, ensuring continuous air renewal and improved indoor air quality compared to VCR systems, which often rely on partial air recirculation; they can achieve very high performance levels, with

* Corresponding author.
E-mail address: nicolo.morselli@unimore.it (N. Morselli).

https://doi.org/10.1016/j.applthermaleng.2026.131197
Received 9 February 2026; Received in revised form 16 April 2026; Accepted 24 April 2026
Available online 27 April 2026

Nomenclature

A	Heat transfer surface area, m^2
COP	Coefficient of performance, –
CSA	Cross-sectional area, m^2
D_H	Hydraulic diameter, m
f	Fanning friction factor, –
$\dot{m}$	Mass flow rate, kg/s
Δp	Pressure difference, Pa
$\dot{Q}$	Heat transfer rate, W
V	Volume, m^3
$\dot{V}$	Volumetric flow rate, m^3/s
Re	Reynolds number, –
ΔT	Temperature difference, $^\circ C$
$\dot{W}$	Mechanical power, W
w	Average fluid velocity, m/s
r	Recirculation rate, –
L	Total HMX length, m
s	HMX wall thickness, m

Greek letters

η	Efficiency, –
ϵ	Effectiveness, –
θ	Measurement uncertainty, –
μ	Dynamic viscosity, $Pa{\cdot}s$
ρ	Density, kg/m^3
ω	Absolute humidity, g_{vap}/kg_{da}
φ	Relative humidity, –

Acronyms	Description
MEX	Material extrusion
HX	Heat exchanger
PWM	Pulse-width modulation
HMX	Heat and mass exchanger
IEC	Indirect evaporative cooling
DEC	Direct evaporative cooling
DPEC	Dew-point evaporative cooling
PLA	Polylactic acid
HTR	Heater
TPMS	Triply Periodic Minimal Surface
VCR	Vapor compression refrigeration

Subscripts

w	Working air
p	Product air
in	Inlet
out	Outlet
atm	Atmospheric
da	Dry air
db	Dry bulb
wb	Wet bulb
dp	Dew point
sat	Saturation
fan	Fan-related terms
$cool$	Cooling
vap	Vapor
$pump$	Pump-related terms

typical coefficient of performance (COP) values in the range of 15–20 [3] and peaks approaching 90 in specific configurations discussed in literature [7].

Despite their potential, evaporative cooling systems generally require larger installation spaces compared to conventional systems [8]. Additionally, they face several practical challenges: their performance strongly depends on ambient humidity, degrading in hot and humid climates [9], and they require a continuous water supply, which can create logistical issues and lead to problems such as mineral scaling or nozzle clogging if not properly managed [10].

A more advanced variant of IEC, is the dew-point evaporative cooling (DPEC), first proposed in 1976 by Valeriy Maisotsenko and known as M-cycle [11]. Its operating principle is illustrated in Fig. 1, where, a cross-flow configuration is shown, consisting of a heat and mass exchanger (HMX) where "mass" highlights the presence of mass transfer, i.e., water vapor exchange, distinguishing it from a conventional heat exchanger (HX). In this arrangement, the hot ambient air (1) flows within the product channel where it is gradually pre-cooled by transferring heat to the adjacent wet surface. At the end of the product channel (2) part of this pre-cooled air is recirculated into the working channel (3′), where water evaporation occurs (3), allowing for the indirect cooling of the incoming air [12].

Since then, several technical implementations have been developed and patented worldwide and some of these patented technologies have been commercialized, most notably by Seeley International [13], which developed and distributed DPEC based air conditioning systems globally [14].

Nevertheless, despite the availability of commercial solutions, ongoing scientific research is still actively addressing key limitations of current systems, particularly in terms of compactness and COP, as discussed in the literature review presented in the following section.

1.1. Literature review

The performance of M-cycle evaporative coolers has been widely investigated in literature, using a variety of approaches (experimental,

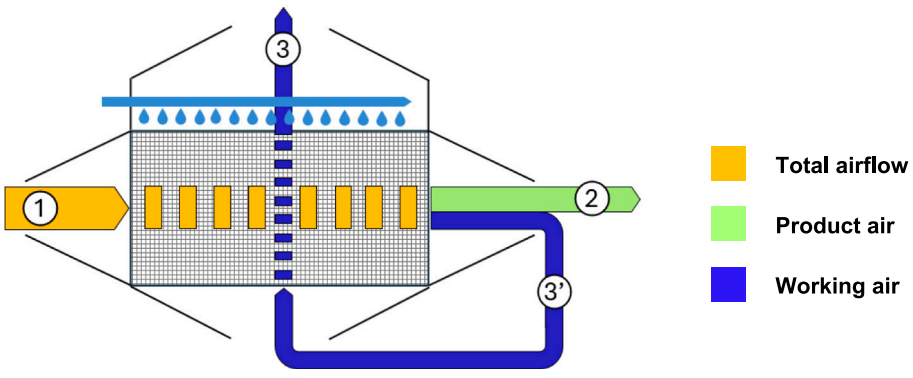

Fig. 1. Schematics of the cross-flow configuration of the M-cycle DPEC HMX.

numerical, analytical, etc.) and testing different HMX configurations.

Comprehensive reviews have been conducted by Dizaji et al. [1] and Alam et al. [6], who mainly categorized the configurations in counter-flow or cross-flow. In the present work, the review focuses on studies concerning cross-flow HMXs to properly contextualize this research within the current state of the art, with particular emphasis on recent efforts investigating the role of geometry in enhancing the performance of M-cycle HMXs through the optimization of channel design, internal structures, and material properties.

For instance, Ali et al. [4] introduced circular aluminum fins in dry channels, increasing the heat transfer area by 5% and achieving a cooling capacity enhancement of 18% (358–1020 W), with supply air temperatures around 16.5 °C, COP values up to 14.58 under optimal input parameters, and effectiveness ranging between ε_{wb}= 126–145% and ε_{dp}= 87–93%. Similarly, Jradi and Riffat [15] numerically optimized a cross-flow psychrometric energy core (PEC) using perforated sheets to gradually divert air into wet channels, identifying optimal dimensions of 5 mm channel height, and then experimentally validating their model. They tested five different fan velocities, obtaining cooling capacities ranging between 1053 and 1247 W, COP values between 5.9 and 14.2, and wet bulb effectiveness values between 70 and 117.

Further geometric refinements include the work of Khalid et al. (2016), who improved the channel width-to-height ratio and employed hydrophilic felt to ensure uniform wettability, achieving ε_{wb} = 92–120% and ε_{dp} = 62–85%, with a 5% efficiency improvement over previous designs. The authors also report on the effect of feed-water temperature (20–24 °C) which affected performance by less than 5%.

Lin et al. (2017) proposed a cross-flow configuration with a dedicated pre-cooling and dehumidification section for the working air, reaching $\varepsilon_{wb}\approx$ 1.25 and $\varepsilon_{dp}\approx$ 0.85, with a COP of 4.6 under humid conditions (potentially increased by 70–135% with upstream dehumidification). Pandelidis et al. [16] compared two cross-flow architectures, showing that small rearrangements in the geometry and flow direction could produce large differences in the performance. In particular, a co-current pre-cooling configuration achieved a specific cooling capacity of 26.6 kW/m^3 and ε_{wb} = 119%, outperforming a modified opposite-inlet design, which reached 21.6 kW/m^3 and ε_{wb}= 97% under 30 °C and 30% relative humidity conditions.

More recent work by Rasheed et al. [17] explored six configurations varying perforation patterns, wetted area, and channel design using low-cost polymeric materials (laminated polypropylene with non-woven fabrics), achieving in the optimal case a cooling capacity of 2.07 kW, COP of 6.91 (EER = 23.59), and effectiveness of ε_{wb} = 1.12 and ε_{dp} = 0.86. Earlier, Zhan et al. [12] systematically compared cross-flow and counter-flow configurations, highlighting the influence of channel height (3–12 mm), length (up to 2.2 m), and air guide geometry; counter-flow systems provided 20% higher cooling capacity and 15–23% higher effectiveness, while cross-flow configurations exhibited lower pressure drops and a theoretical COP up to 530, which clearly indicates a likely oversizing of the heat exchanger.

For a clearer visualization of the reviewed studies the following table is reported.

These studies show that current research mainly pursue incremental geometric refinements, such as adjustments in channel dimensions, surface features, flow distribution, and wettability, within conventional plate-based designs. Whereas the approach proposed here moves beyond the paradigm of parallel-plate architectures by introducing the first application of Triply Periodic Minimal Surfaces (TPMS) to the Maisotsenko cycle. Although TPMS geometries have gained significant interest in single-phase heat transfer for their superior fluid-mixing properties and early transition to turbulent regime, their potential in heat and mass transfer for evaporative coolers remains largely unexplored in current literature. This work addresses this gap by providing first-of-its-kind experimental evidence of a gyroid-based M-cycle cooler, shifting the focus from 2D surface modifications to a fundamentally different 3D heat transfer topology.

1.2. TPMS heat exchangers applied to evaporative coolers

TPMS constitute a class of implicit surfaces characterized by three-dimensional periodicity, zero mean curvature, and a high surface to volume ratio [18]. These geometries can be accurately represented through mathematical equations, enabling direct control of structural parameters such as porosity (defined as the ratio of void to solid volume) and specific surface area. Thanks to additive manufacturing it has become possible to physically fabricate these complex structures with high precision, translating the mathematical designs into real, functional components.

When appropriately designed, TPMS structures divide the domain into two separate regions connected by a single, continuous heat transfer surface, thus facilitating the design of cross-flow HX. A comprehensive description of the governing equations for the most common TPMS geometries is well reported by Reynolds et al. [19].

The interest in TPMS-based HXs has been steadily increasing, since such surfaces can induce an earlier transition to turbulent flow compared to conventional geometries [20] and this tendency, combined with the inherently high surface to volume ratio, provides a promising opportunity to enhance heat transfer performance respect of traditional HX configurations [21]. In IEC, the dry channel typically represents the bottleneck in terms of heat transfer due to the high convective thermal resistance which limits the compactness of these HMX. In this context, TPMS structures could play a significant role due to the enhanced flow mixing that occurs even at low velocities which increases the specific heat transfer coefficient. In the same way, on the wet side of the HMX, the main benefit may arise from enhanced interaction between the two phases present (air and water).

Among the available TPMS geometries, the gyroid structure is particularly noteworthy, as it is already recognized for its favorable thermo-hydraulic efficiency [22]. Originally identified by Alan Schoen in 1970 [23], the gyroid belongs to the class of TPMS with cubic symmetry, a feature that makes it especially suitable for heat and mass transfer applications and despite the growing body of literature on TPMS-based heat exchangers, their application to evaporative cooling remains limited. The same authors have experimentally tested an

Author	T_{in} [°C]	ε_{wb} [%]	ε_{dp} [%]	COP	Cooling capacity [W]	Inlet air humidity [g/kg$_{da}$]	Inlet air velocity [m/s]	Inlet flow rate [m^3/h]	Heat exchanger dimensions [mm]	r
Ali et al.	30–45	126–145	87–93	7.15–14.58	358–1020	10–12	2–6	2000	–/480/900	0.3
Jradi et al.	26.1–41.1	70–117		5.9–14.2	1054–1246.7	6.6–8	0.36–1.85	300–1500	850/750/600	0.33
Khalid	25–45	92–120	62–85		30–270	11–19	0.49–1.1		508/203/157	0.3
Lin et al.	25–37	86–125	85	4.6	2200	12–13-17.6	1.4–1.6	2800	400/132/72	0.45
Pandelidis et al.	18–45	97–135	–	–	14.7–26.6[a]	7.9–13.3	3	150–800	–	0.5
Rasheed et al.	45	29–112	22–86	6.91	2070	13	5.6	320	300/410/204	0.26
Zhan et al.	28	113.9	75.7	530	2994	11.35	2.4	2000 m^3/h	1000/1000/1000	0.5

[a] This value is expressed in kW/m^3, as it was reported as specific cooling capacity by the author.

indirect evaporative heat exchanger based on gyroid structures [24] marking the first documented experimental investigation of TPMS and in particular the gyroid geometry, applied to indirect evaporative cooling (IEC). While previous research had focused exclusively on TPMS heat exchangers under "dry" conditions, this pioneering work demonstrates that such structures can achieve a volumetric cooling capacity of up to 129 kW/m^3, approximately three times higher than conventional aluminum cross-flow plate exchangers. The study also highlights how the high surface-to-volume ratio of the gyroid morphology enables wet-bulb efficiencies up to 90% even when using untreated hydrophobic polymeric materials (PLA), showing that geometric complexity can compensate for low material wettability and overcome the performance limits of standard parallel-channel architectures.

However, the application of TPMS geometries to M-cycle configurations has not yet been experimentally investigated.

The following section describes the TPMS-based HMX and the experimental setup, while the subsequent sections introduce the governing equations used to evaluate performance and discuss the results obtained.

2. Experimental setup

2.1. Investigated TPMS heat and mass exchanger in M-cycle configuration

The HMX has an overall cubic geometry with external dimensions of 100 × 100 × 100 mm and consists of six elementary gyroid cells per side, resulting in a unit cell size of 16.67 mm. The gyroid structure was generated using MSLattice [25] by imposing a relative density of 15% and a mesh density of 30 points, which led to an average wall thickness of approximately 0.8 mm.

The selected cell size yields a hydraulic diameter ($D_H = \frac{4V_{channel}}{A}$) of 9.16 mm, which was chosen to mitigate clogging phenomena caused by water surface tension effects. As observed in previous work, excessively small hydraulic diameters, in the absence of hydrophilic surface treatments, can promote flow blockage and unstable wetting behavior [24].

A flanged support structure was designed around the gyroid HMX to enable secure bolted integration with the experimental test bench. The additive manufacturing technology employed for this purpose was material extrusion (MEX) where the minimum wall thickness selected allowed for two nozzle passes, which enhance the specimen's airtightness, at the cost of a slight increase in the wall's conductive thermal resistance. The specimens were manufactured using a Sharebot Model 43 printer and a Sharebot PLA filament with a layer height of 0.2 mm, selected for its ease of printing despite its limited suitability for operation in humid environments. Since the purpose of this work was to experimentally assess the fluid dynamic and thermal behavior of the proposed geometry rather than to optimize the final material for industrial application, PLA was considered an adequate choice for the prototype fabrication. To repair possible porosities or cracks and to mitigate the hygroscopic nature of the material, the wet channel was sealed with a sprayable waterproofing agent. The tightness was then verified by filling the wet channel with water and ensuring that no leakage occurred into the dry channel.

Fig. 2 shows a 3D representation of the HMX and a photograph of the HMX section, while Table 1 reports the geometrical dimensions of the HMX, including: the net volume of a single channel of the HMX ($V_{channel}$), D_H, the cross section area ($CSA = \frac{V_{channel}}{L}$) and the heat transfer surface area (A) calculated through the STL file.

2.2. Description of the test rig

The experimental setup allows testing of cross-flow TPMS HMX operating according to the M-cycle scheme, as illustrated in the P&ID of Fig. 3 and pictures in Fig. 4.

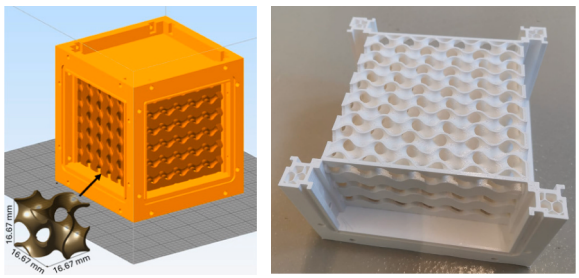

Fig. 2. (a) MSLattice representation of the elementary cell with the reference dimensions reported in Table 1 and a Simplify3D visualization of the assembled HMX ready to print; (b) photograph of the section of the heat exchanger used together with the supporting structure.

Table 1
Geometrical parameters of the TPMS structures.

Parameter	Value	Unit
Wall thickness (s)	0.8	*mm*
Base unit length	8.335	*mm*
Elementary cell length	16.67	*mm*
Elementary cell repetition for the HMX (x*y*z)	6x6x6	*units*
HMX total length (L) in the flow direction	100	*mm*
Net volume of a single channel	431,462	mm^3
Total porosity	43.1462	%
HMX volume	$1{\cdot}10^6$	mm^3
A	188,470	mm^2
CSA	4315	mm^2
D_H	9.16	*mm*

The HMX is installed downstream of an intake plenum volume of 30 L designed to homogenize the velocity profile and the thermophysical properties of the incoming air. The air is motivated through the system by a PWM-controlled centrifugal blower (FAN in Fig. 3) that draws ambient air and delivers it to an electrical heater (HTR), also PWM-controlled. This configuration allows a precise regulation of both the inlet volumetric flow rate ($\dot{V}_{in}$) and the inlet air temperature T_{in}. The control system is managed by an Arduino UNO microcontroller unit and MOSFET drivers. The ambient temperature and humidity conditions are monitored using a Testo 0636–9732 thermo-hygrometric probe wire-connected to a Testo 440 datalogger.

The HMX is connected to the plenum through the dry channel inlet, where no humidification occurs and indirect cooling takes place through the heat transfer surface separating dry and wet channel. In the M-cycle, a portion of the air leaving the dry channel is diverted and recirculated through the wet channel, forming the *working air* (subscript *w*). The working air passes through the second channel of the HMX, whose internal surfaces are continuously kept wet by distilled water sprayed from a membrane pump. The pump draws the water from a tank where the excess water is recovered and runs on a programmed duty cycle of 0.5 s ON and 5 s OFF. A T-type thermocouple is used to keep the water temperature monitored.

At the wet channel outlet, the humidified working air is characterized in terms of volumetric flow rate ($\dot{V}_w$) using a Testo 417 vane anemometer positioned ten duct diameters downstream the HMX, with a flow straightener installed to further uniformize the velocity field.

The dry-bulb and wet-bulb temperatures are measured by two 1/10 DIN precision PT100 RTDs (model SE012 by Pico Technology - 4 mm diameter); the wet-bulb probe is wrapped in a cotton wick kept moist through periodic injection of distilled water and its operation was verified over the range of tested air velocities using the Testo thermo-hygrometer. All temperature data are acquired by a Pico PT104 datalogger.

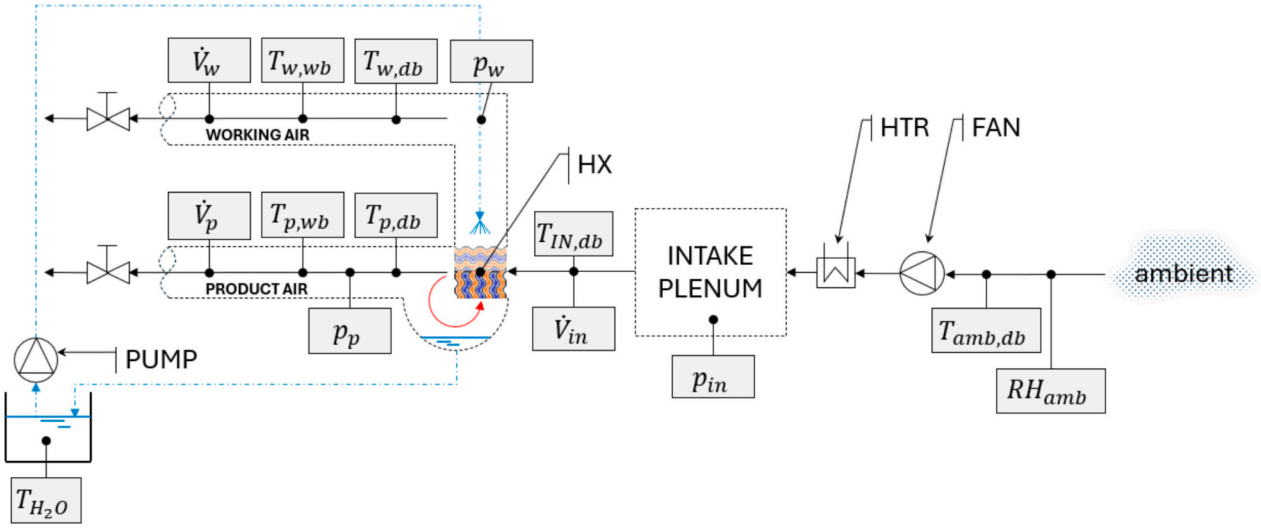

Fig. 3. P&ID diagram of the test bench with indications of the measured parameters.

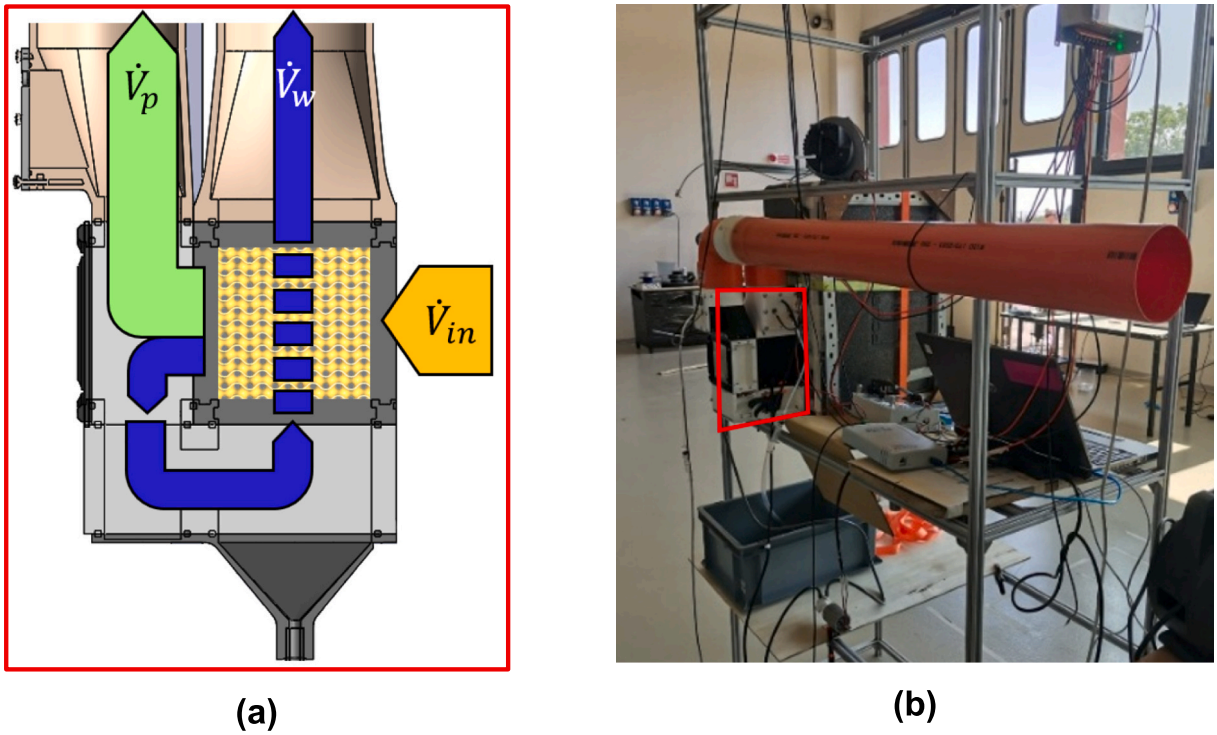

Fig. 4. (a) CAD section of the tested prototype connected to the test bench, showing the total (yellow), the product (green) and working (blue) air flow paths; (b) photograph of the experimental test bench with the test section highlighted in red.

The same set of measurements, performed with identical instrumentation, are carried out on the airflow leaving the dry channel, referred to as *product air* (subscript *p*). At the outlets of dry and wet channels iris valves are installed to control the portion of air recirculated in the wet channel. The inlet air volumetric flow rate can be varied from 35 to 65 m^3/h and its temperature from 25 °C to 35 °C, while the inlet air humidity cannot currently be modified as it is controlled by the laboratory HVAC system where the tests are performed.

2.3. Adopted methodologies

2.3.1. Fluid dynamic characterization

For complex geometries such as gyroid-based TPMS structures, a dimensionless fluid dynamic analysis is required to characterize the operating flow regime. This is achieved by nondimensionalizing the governing quantities, primarily through the Reynolds number (*Re*) and the Fanning friction factor (*f*), which describes the distributed pressure losses along the structure [26].

It should be noted that the *Re* defined in Eq. (1) refers to fluid properties such as density (ρ) and dynamic viscosity (μ) evaluated at the mean fluid temperature by interpolating tabulated data [27]. The hydraulic diameter is used in its volume-averaged form, since it varies continuously along the structure and the classical formulation for constant section ducts is not suitable for the case. D_h can be represented in several ways that converge on the one reported in Eq. (2) [28].

$$Re_H = \frac{\rho w D_H}{\mu} \tag{1}$$

$$D_H = \frac{4V_{channel}}{A} \tag{2}$$

The average velocity of the airflow inside each channel (w) was obtained by dividing the mean volumetric flow rate by the *CSA*, calculated from the ratio between $V_{channel}$ and the total length L of the HMX.

$$w = \frac{\dot{V}}{CSA} \tag{3}$$

$$CSA = \frac{V_{channel}}{L} \tag{4}$$

The Fanning friction factor is calculated, for dry and wet channel, according to Eq. (5) where Δp is the pressure drop across each of the two channels of the M-cycle, referenced to the mean air velocity and density in each channel. With reference to the diagram in Fig. 3, the pressure drop in the dry channel is given by $\Delta p_p = p_{in} - p_p$, while the pressure drop in the wet channel is $\Delta p_w = p_p - p_w$.

$$f = \frac{\Delta p\, D_H}{2\rho w^2 L} \tag{5}$$

2.3.2. Heat transfer characterization

A comprehensive overview of the parameters that must be considered when assessing the thermodynamic performance of DPEC systems was provided in the work by Alam et al. [6]. Based on this, the following criteria have been evaluated.

The temperature drop ΔT_p is the difference between the inlet and outlet dry bulb temperatures of the product air.

$$\boldsymbol{\Delta T_p = T_{p,db,in} - T_{p,db,out}} \tag{6}$$

Since the performance of IEC (and by consequence, also of DPEC) strongly depends on the capability of the wet channel to evaporate water, the effectiveness ε can be expressed in two different ways, depending on the reference temperature (wet bulb or dew point). Wet-bulb and dew-point effectivenesses are calculated as the ratio between the dry-bulb temperature difference across the device (inlet-outlet) and the corresponding difference between the inlet dry-bulb temperature and the inlet wet-bulb or dew-point temperature as reported in Eq. (7) and (8).

$$\varepsilon_{wb} = \frac{T_{p,db,in} - T_{p,db,out}}{T_{p,db,in} - T_{p,wb,in}} \tag{7}$$

$$\varepsilon_{dp} = \frac{T_{p,db,in} - T_{p,db,out}}{T_{p,db,in} - T_{p,dp,in}} \tag{8}$$

In M-cycles, it is common to investigate the behavior of the HMX as the recirculation rate of the air into the wet channel is varied. This recirculation rate r is calculated as the ratio between the mass flow rate of the working channel $\dot{m}_w$ and the total mass flow rate at the HMX inlet $\dot{m}_{in}$, which corresponds to the flowrate in the dry channel:

$$r = \frac{\dot{m}_w}{\dot{m}_{in}} \tag{9}$$

Since in the proposed configuration the fluid (moist air) must be treated as a two-phase mixture, these and the following quantities need to be referenced to the two components of the mixture (dry air and water vapor) following a psychrometric approach.

Using the measured dry-bulb and wet-bulb temperatures ($T_{p,db}$, $T_{p,wb}$), along with air velocity for both the product and working air streams, the density and mass flow rate of dry air (subscript *da*) were determined. For brevity, the equations are presented for the dry channel only, as the same procedure applies to the working channel.

The dry air density $\rho_{da,p}$is calculated from Eq. (10) by applying Dalton's law for partial pressures and the ideal gas law.

$$\rho_{da,p} = \frac{p_{atm} - p_{vap,p}}{287} \cdot \left(T_{p,db} + 273.15\right)$$

where

$$p_{atm} = p_{da} + p_{vap} \tag{10}$$

Where the vapor pressure $p_{vap,p}$ and the saturation pressure $p_{sat,p@Tdb}$ are calculated respectively according to Eq.(11) and the Magnus-Tetens equation (Eq. (12)), while the air relative humidity φ_p is calculated through the Assman equation (Eq. (13)).

$$\mathrm{p_{vap,p}} = \frac{\mathrm{p_{sat,p}} \cdot \varphi_\mathrm{p}}{100} \tag{11}$$

$$\mathrm{p_{sat,p@Tdb}} = 610.5 \cdot \mathrm{e}^{\frac{17.269 \cdot \mathrm{T_{p,db}}}{237.3 + \mathrm{T_{p,db}}}} \tag{12}$$

$$\varphi_p = \frac{p_{sat,p@Twb} - 0,00066 \cdot 101325 \cdot \left(T_{p,db} - T_{p,wb}\right)}{p_{sat,p@Tdb}} \tag{13}$$

The dry air mass flow rate $\dot{m}_{da}$ is thus calculated through the measured $\dot{V}_p$:

$$\mathrm{\dot{m}_{da,p}} = \rho_{\mathrm{da,p}} \cdot \mathrm{\dot{V}_p} \tag{14}$$

The cooling capacity is found as the difference between the mixture specific enthalpy of the incoming air and the mixture enthalpy of the air leaving the system and it is the amount of heat that the system can remove from the product air by evaporating water within the wet channel:

$$\dot{Q}_{cool} = \left(h_{p,db,in} - h_{p,db,out}\right) \cdot (1 - r) \cdot \dot{m}_{in} \tag{15}$$

Where the mixture enthalpy can be calculated as follows:

$$h = 1.005 \cdot T + \omega(2501.3 + 1.82 \cdot T) \tag{16}$$

With the absolute humidity calculated as:

$$\omega = \frac{m_{vap}}{m_{da}} = 0.622 \frac{p_{sat@T}\, \varphi}{p_{atm} - p_{sat@T}\, \varphi} \tag{17}$$

Water pumping power was not considered in the *COP* calculation due to its extreme variability, ranging from high-pressure, atomization-based systems to pumpless configurations relying on capillary action. The fan power consumption was accounted for and evaluated as $\dot{W}_{fan} = \frac{\dot{V}_{in}\, \Delta p_p + \dot{V}_w\, \Delta p_w}{\eta_{fan}}$ where $\dot{V}_{\mathrm{in}}$and $\dot{V}_w$ are the volumetric flow rates in the dry and wet channels, respectively, and $\Delta p_p$and $\Delta p_w$are the corresponding pressure drops. The fan overall efficiency was assumed to be equal to 0.5.

$$\mathrm{COP} = \frac{\dot{\mathrm{Q}}_{\mathrm{cc}}}{\dot{\mathrm{W}}_{\mathrm{fan}}} \tag{18}$$

2.3.3. Uncertainty analysis

In data processing, each computation contributes to the overall measurement uncertainty. This cumulative effect was quantified using the procedure described by Kline and McClintock [29], a well-established method in experimental research. In this approach, the calculated result R is expressed as a function of a set of independent variables $(x_1, x_2, \ldots, x_n)$ (Eq. (19)), where each variable is characterized by its own absolute uncertainty $(\theta_1, \theta_2 \ldots, \theta_n)$, as reported in Table 2 for each of the instruments used. The resulting propagated uncertainty,

Table 2
Uncertainty range of the instrument used.

Instrument	Resolution		Accuracy	
Thermo-anemometer	0.01	m/s	$\pm(0.1+1.5\%_{mv})$	m/s
Testo mod. 417	0.1	$^{\circ}C$	±0.5	$^{\circ}C$
Differential micromanometer Chauvin Arnoux CA 1550	0.1	Pa	$\pm(0.5\%_{mv}+1)$	Pa
Thermo-igrometer	0.1	$\%_{RH}$	±0.5	$\%_{RH}$
Testo 0636–9732	0.1	$^{\circ}C$	±0.5	$^{\circ}C$
Platinum resistance thermometer Pico Technology mod. SE012	0.01	$^{\circ}C$	$\pm0.03@0^{\circ}C \pm 0.07@50^{\circ}C$	$^{\circ}C$

indicated as θ_R, is then evaluated according to Eq. (20)

$$\boldsymbol{R} = \boldsymbol{f}(\boldsymbol{x_1}, \boldsymbol{x_2}, \ldots, \boldsymbol{x_n}) \tag{19}$$

$$\theta_R = \left[\left(\frac{\partial R}{\partial x_1}\theta_1\right)^2 + \left(\frac{\partial R}{\partial x_2}\theta_2\right)^2 + \ldots + \left(\frac{\partial R}{\partial x_n}\theta_n\right)^2\right]^{\frac{1}{2}} \tag{20}$$

2.3.4. Design of experiments

The performance of the gyroid HMX operating in M-cycle configuration was investigated under controlled variations of three operating conditions: (i) the total airflow rate through the dry channel, controlled via the fan duty cycle; (ii) the recirculation rate r; and (iii) the effect of different inlet-air temperatures at constant absolute humidity, which therefore resulted in different levels of relative humidity.

The total airflow rate was adjusted by acting on the duty cycle of the fan through a pulse-width-modulated (PWM) signal. The PWM values were discretely varied and set to 180 and 255, corresponding respectively to 71% and 100% of the fan duty cycle. This modulation allowed different velocity ranges inside the HMX to be investigated. The recirculation rate was regulated by operating the iris valves covering a range of r values from 0.75 down to 0.20. The inlet air temperature was controlled by modulating the PWM of the electrical resistor, selecting two temperature setpoints, 30 °C (φ = 43%) and 35 °C (φ = 32%).

This experimental plan resulted in a full factorial design, in which all 32 combinations of fan PWM, inlet-air temperature, and recirculation rate were tested.

The performance of the gyroid DPEC unit was evaluated for each experimental condition by calculating the product-air temperature, cooling capacity, coefficient of performance, wet-bulb effectiveness, and water consumption.

Before each test, the inlet air temperature setpoint and the fan PWM were first adjusted to the desired values, and both wet-bulb probes were manually humidified to ensure complete saturation of the wick. The system was then operated at steady state for 15 min and, once stabilization was achieved, temperature, air-velocity, and pressure data were logged. The two iris valves were then repositioned to achieve the next recirculation-rate value prescribed in the experimental matrix. At the beginning of each new acquisition, the wet-bulb probes were humidified again to maintain consistent wet-bulb temperature measurements throughout the test series.

3. Experimental results

3.1. Fluid dynamic characterization

From the measured pressure drop and volumetric flow rate, and based on Eqs. (1) and (5), the Fanning friction factor diagram as a function of the Reynolds number was reconstructed and reported in Fig. 5. The trend of the friction coefficient provides relevant information on the flow regime inside both the dry and wet channels, allowing the HMX performance to be interpreted in relation to the operating flow conditions.

The results show a clear stabilization of f in the dry channel at values close to 1, indicating that the flow regime was turbulent and fully developed across the entire range of investigated Re. In the wet channel, characterized by lower velocities, the friction factor approaches higher asymptotic values, approximately equal to 1.2, but only for Reynolds numbers above 700, suggesting that the fully developed regime is reached only beyond this threshold. It should be noted, however, that the experimental uncertainty is relatively large-particularly due to flow-rate measurements, which introduces scatter in the calculated f and may partially blur the exact transition region.

This behavior is consistent with the available literature, which indicates the onset of fully turbulent flow at $Re \approx 1000$. The values obtained in this study therefore fall within experimental uncertainty and are in good agreement with previously reported results.

Furthermore, all data points fall within the range reported by Reynolds et al. as indicated by the dashed lines on the graph; these reference curves describe the behavior of gyroid HMX with hydraulic diameters ranging from 7.5 mm to 10 mm, while, in the present study D_H = 9.16 mm.

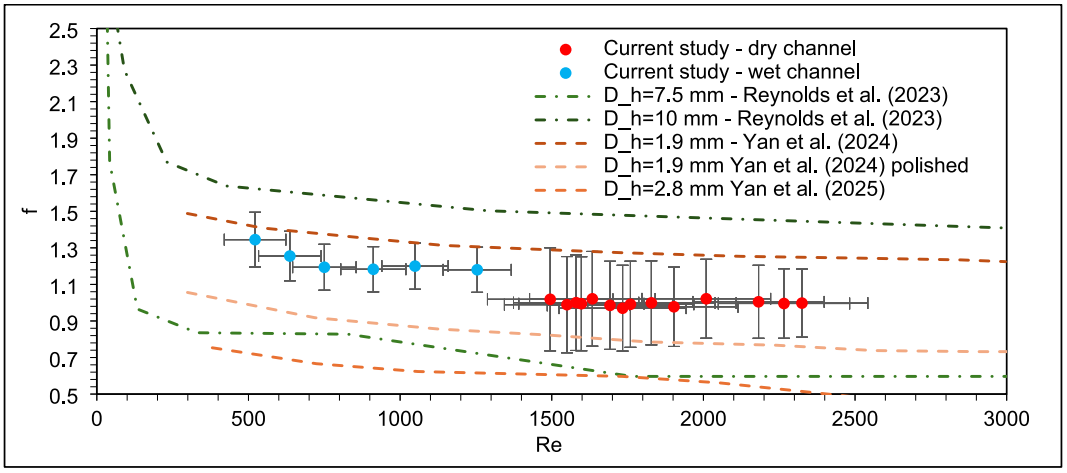

Fig. 5. Fanning friction factor as a function of the Reynolds number for the dry channel (red symbols) and the wet channel (blue symbols). The dashed lines represent the limits found in literature by Reynolds et al. [19] and Yan et al. [28,30], regarding the behavior of gyroid heat exchangers with hydraulic diameters ranging from 7.5 mm to 10 mm. (For interpretation of the references to colour in this figure legend, the reader is referred to the web version of this article.)

Regarding the robustness of the present definition of the friction factor, an important remark must be added: the friction-factor diagram also includes values reported by Yan et al. [28], which were obtained for gyroid structures characterized by significantly smaller hydraulic diameters than those used in the present study (i.e., 1.9 and 2.8 mm). The purpose of including these data is to highlight that defining a friction factor that is universally valid for all gyroid geometries is still not straightforward, as different additive-manufacturing techniques and surface-finishing processes can strongly affect the results.

For this reason, the f values reported by Yan et al. for internally smoothed gyroid structures were also included. As expected, these data clearly show that surface roughness plays a major role in determining the friction factor and must therefore be considered when comparing different studies. This comparison underlines the importance of providing an explicit evaluation of f in each experimental investigation, rather than relying on generalized correlations.

3.2. Thermodynamic characterization

The thermodynamic characterization, as described in Section 2, followed a psychrometric approach and led to the evaluation of several performance indicators. A first level of analysis was conducted by assessing the temperature drop produced by the HMX, quantified as in Eq. (6).

Fig. 6a reports the dry-bulb temperature reduction of the product air, $\Delta T_{db,out}$, as a function of the recirculation rate r for two different fan duty cycles at an inlet air temperature of 30 °C. In the callouts reported in the figure, the maximum and minimum values of the average fluid velocity in the dry channel are indicated to highlight the contribution of the two different PWM settings and the resulting test range. These data are not reported in the following figures, as they are derived from the same experimental tests.

A solid monotonic increasing trend (in absolute value) is observed: as expected, the temperature drop becomes larger as the recirculation rate increases. This behavior is consistent with the physical interpretation of the M-cycle principle where higher r increase the fraction of air flowing in the wet channel, both promoting the interaction between the fluid and the wetted surface (higher specific mass transfer coefficient), thereby enhancing evaporation.

At any given recirculation rate, the lower fan speed (PWM 180) consistently produces a larger temperature drop than PWM 255. This appears to be a natural consequence of both the reduced mass flow rate and the already turbulent nature of the flow ensured by the TPMS, which seems to promote high mass and heat transfer even at low Reynolds numbers. Furthermore, the ΔT increase tends to flatten as r increases, however, this effect is much less pronounced than in longer HMX, where ΔT typically becomes weakly dependent on r beyond values of approximately 0.5 [9]. In the present case, the limited length of the HMX partially hinder the expected asymptotic behavior, where the temperature difference progressively flattens as the outlet air conditions approach the dew-point temperature.

It also can be noted that the distance from the dew-point temperature (≈16 °C for all the tests performed) shifts the max ΔT limit to much lower values than those obtained, indicating that, while the small-scale geometry certainly plays a role, the conductive resistance of the polymer used also affects performance. Moreover, the ΔT value obtained at PWM 180 for $r \approx 0.37$ is comparable to that obtained at PWM 255 for $r \approx 0.7$, suggesting potential efficiency optimization strategies when the product air temperature outlet is the target.

In incrementing the inlet temperature to 35 °C (Fig. 6b), the concurrent reduction in average relative humidity (from 43% to 32%) increases the vapor pressure gradient between the water film (assuming saturation conditions) and the bulk flow in the humid channel, thereby enhancing mass transfer and promoting evaporation. This effect is expected and consistent with literature, and it results in a increase in ΔT, which rises from 4.7 °C to 6.1 °C under nearly identical recirculation conditions ($r \approx 0.7$).

During all the experimental tests, the water temperature remained nearly constant, with an average value of 23.5 °C, a minimum of 22.6 °C, and a maximum of 25.7 °C; such variations are sufficiently small that they do not produce appreciable effects on the results within the experimental measurement uncertainty.

The cooling capacity is reported Fig. 7a and b. Also due to the limitation of the test bench, that sets the minimum $r \approx 0.2$, from the tests it is not observed the typical decrease in cooling capacity for r values approaching to 0. It is anyway visible a plateau in $\dot{Q}_{cool}$ for the lowest r tested suggesting that the peak is likely located in close proximity. This result is consistent with the behavior of DPECs where ΔT increases together with the recirculation rate but the increase in ΔT remains less than proportional to the reduction in the outlet mass flow rate of the dry channel, generating lower cooling capacities.

In the literature, there is a wide variability in the value of r at which the peak cooling capacity is achieved. This variability strongly depends on environmental conditions, HMX geometry and flow rate, making direct comparisons with standard geometries difficult (see Chu et al., (2021) [7]; Duan et al., (2017) [8]).

Nevertheless, it is noteworthy that no distinct maximum peak is observed even under low flow-rate conditions (PWM180), where, under

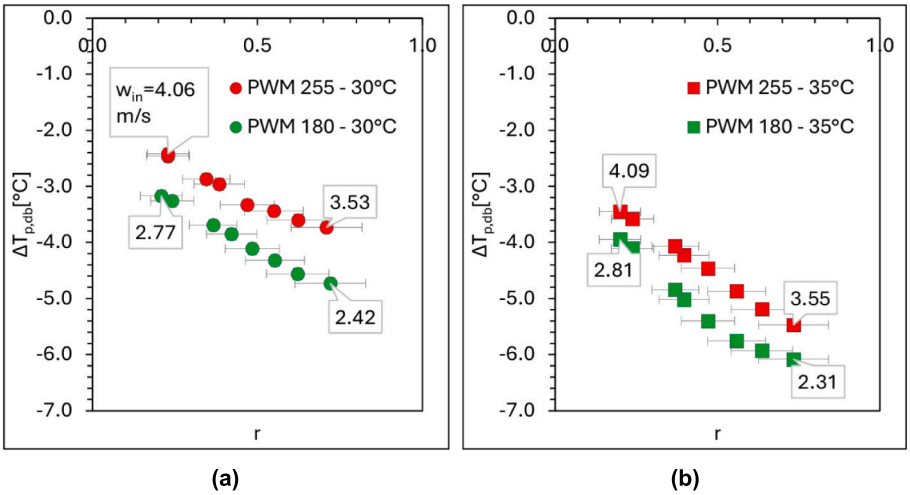

Fig. 6. Dry-bulb temperature reduction of the product air, $\Delta T_{db,out}$, as a function of the recirculation ratio r at an inlet air temperature of 30 °C **(a)** and 35 °C **(b)** for two fan duty cycles (PWM 180 and PWM 255). Callouts indicate the minimum and maximum average air velocities in the dry channel.

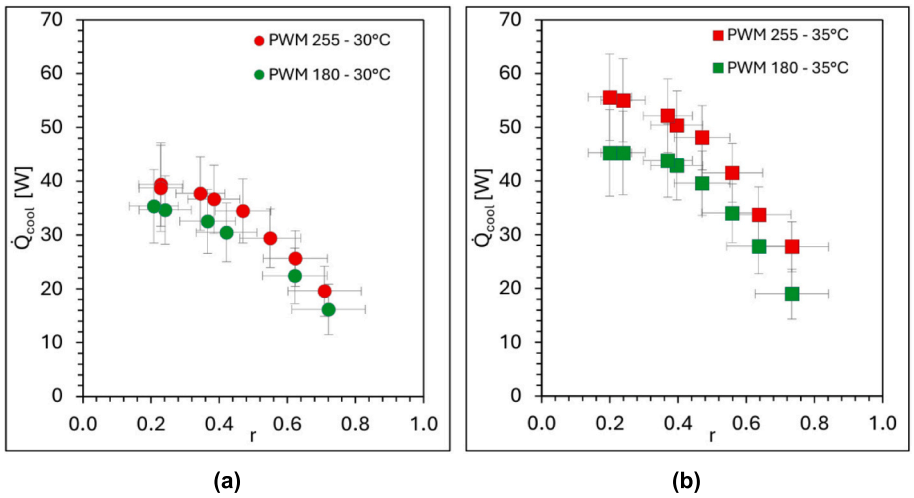

Fig. 7. Cooling capacity $\dot{Q}_{cool}$ as a function of the recirculation ratio r at an inlet air temperature of 30 °C **(a)** and 35 °C **(b)** for two fan duty cycles (PWM 180 and PWM 255).

such conditions, one would expect a shift of the peak toward higher r values as the total flow rate decreases, due to the reduced thermal capacity and the lower effectiveness of mass transfer in the wet channel.

It is therefore likely that the use of a TPMS structure, such as the gyroid, which promotes early boundary-layer disruption through a continuous *split-and-merge* flow behavior, also enhances mass transfer, maintaining its effectiveness even at relatively low flow velocities of the working air. Moreover, in this setup, the low thermal conductivity of the wall material may also play an important role in this interpretation, as the dominant bottleneck of the process is likely the conductive thermal resistance rather than evaporation and convection resistances. Consequently, increasing the wall thermal conductivity would be expected to allow the peak in cooling capacity to be shifted to still lower values of r.

The increase in total processed flow rate produces more pronounced effects in the case with an inlet temperature of 35 °C, with an average increase of 24%, compared to 17% for the case with an inlet temperature of 30 °C.

The maximum cooling capacity reached 55.6 W and 39.4 W under maximum flow-rate conditions (PWM 255) for inlet temperatures of respectively 35 °C and 30 °C, corresponding to volumetric power densities of 55.6 kW/m^3 and 39.4 kW/m^3 referred to the HMX net volume.

To make a comparison with the current literature, for counter-flow DPEC, Chu et al. (2021) [7] achieved a volumetric capacity of approximately 21 kW/m^3 and similarly, Duan et al. (2017) [8] reported a volumetric capacity of about 17 kW/m^3. Lower but still significant values were presented by Lee (2013), with a volumetric capacity of 8.3 kW/m^3, and by Duan et al. (2016) [31], who reported approximately 6.7 kW/m^3.

Cross-flow technologies generally exhibit reduced volumetric capacities: Ali et al. (2021) [4], analyzing a cross-flow DPEC with finned channels, reported a volumetric capacity of 7.4 kW/m^3, which is comparable to the lower range of counter-flow systems, while Jradi and Riffat (2014) [15] reported a markedly lower volumetric capacity of about 3.2 kW/m^3. It should be noted that the environmental conditions in the cited studies are often different and in some cases more favorable than those of the present tests, which limits a direct comparison but still provides a useful framework to contextualize the present results.

However, the result reported by Pandelidis [32] is particularly noteworthy, as a volumetric cooling capacity in the range of 4–14 kW/m^3 and COP between 40 and 65 were calculated under inlet temperature and relative humidity conditions comparable to those of the present study.

It can therefore be observed that the gyroid-based geometry operates within a higher range of volumetric cooling capacity compared to standard geometries. Considering the standard operating conditions at 30 °C with a recirculation ratio of 0.24, a volumetric cooling capacity of 34.7 kW/m^3 is achieved, corresponding to a generated temperature drop of 3.3 °C and a COP of 7.4.

The overall measurement uncertainty, evaluated through error propagation, is relatively high and is mainly driven by the uncertainty associated with the volumetric flow rate measurements. Also this limitation hinders a further reduction of the airflow rates, thereby preventing the investigation of additional operating scenarios.

Fig. 8a and b show the trend of the COP as a function of the recirculation ratio for the two inlet temperatures. In both cases, the COP decreases as the recirculation ratio increases, reaching its highest values at low r. This behavior is observed for both fan speeds and is particularly evident at the lower inlet velocity (PWM 180), which consistently yields higher COP values, reaching the top of 9.1 at 35 °C and $r = 0.2$.

At low recirculation ratios, $\dot{Q}_{cool}$ remains relatively high thanks to the efficient heat and mass transfer promoted by the TPMS geometry, while the electrical power required by the fans is significantly reduced. As the recirculation rate increases, the gain in cooling capacity does not compensate for the higher auxiliary power consumption associated with increased airflow rates, resulting in a progressive reduction of the COP with a steeper decrease from $r > 0.4$.

Similar considerations can be extended to the two inlet temperatures investigated. It is also reasonable to expect the presence of a peak at recirculation ratios slightly lower than the minimum value of r explored in the present experiments.

In the tests conducted at PWM 255, COP values are even lower than those achievable with conventional VCR systems are obtained. This suggests that the optimal operating velocities for gyroid-based configurations are likely closer to the lower end of the range investigated in this study, and therefore around or slightly above 2.5 m/s. Higher velocities, even up to 6 m/s, as commonly reported in the literature [4] for traditional geometries (uniform cross-section channels, often rectangular), should not be taken as a direct reference in this case, given the fundamentally different flow characteristics established within TPMS structures.

The COP values measured for the gyroid-based HMX are significantly lower than those typically reported in the literature for prototypal heat exchangers, while it is worth noting that commercial evaporative coolers generally exhibit COP values in the range of 6–11. For instance, Chu et al. (2021) [7] reported COP values up to 52.5 for a counter-flow dew point evaporative cooler, whereas Kashyap et al. (2021) [9] measured COP values exceeding 60 in regenerative mode and approaching 90 under favorable humidity conditions.

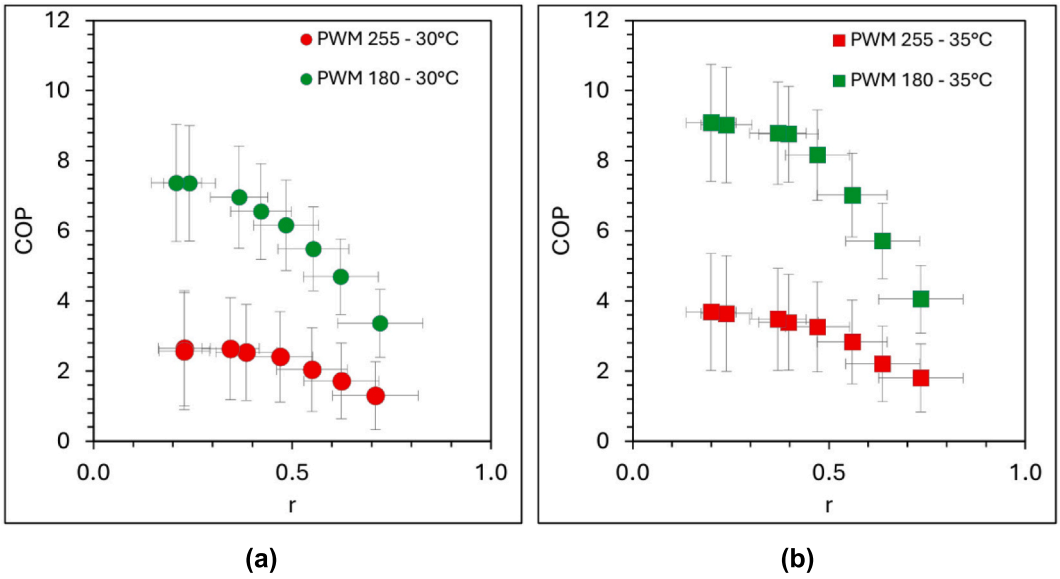

Fig. 8. Coefficient of Performance (COP) as a function of the recirculation ratio *r*at an inlet air temperature of 30 °C **(a)** and 35 °C **(b)** for two fan duty cycles (PWM 180 and PWM 255).

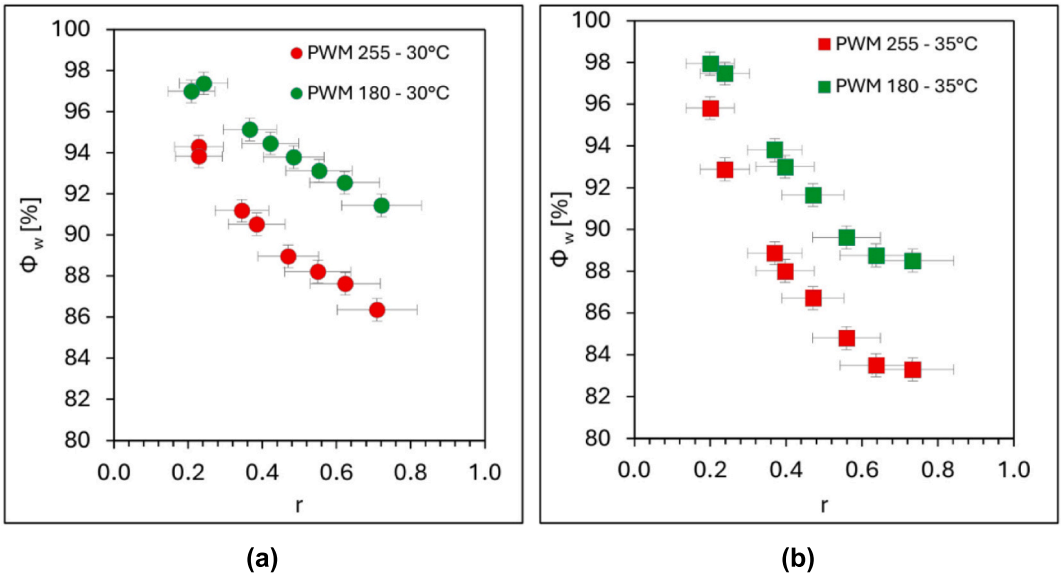

Fig. 9. Outlet relative humidity of the working air stream in the wet channel as a function of the recirculation ratio *r*at an inlet air temperature of 30 °C **(a)** and 35 °C **(b)** for two fan duty cycles (PWM 180 and PWM 255).

Fig. 9a,b report the outlet relative humidity of the working air stream flowing in the wet channel. For each recirculation rate and fan speed, the measured values are always higher than 83% (the minimum recorded value is 83% for PWM 255 at 35 °C with $r = 0.73$). This indicates that the adopted TPMS structure is able to sustain strong evaporation even on untreated surfaces.

This outcome is also supported by the presence of a counter-flow water spray, a configuration that has been reported in the literature [33] to be beneficial for humidification effectiveness.

When comparing the results obtained at different inlet temperatures, it is observed that the peak values recorded at low *r* are comparable for 30 °C and 35 °C and are all close to saturation. As *r* increases, however, the tests conducted at 35 °C exhibit a steeper decrease in relative humidity, with naturally lower values observed for the tests performed at higher flow velocities. In continuity with the previous results related to the dry channel, it can be observed that introducing asymmetry between the two channels is more beneficial. In particular, allocating a greater length to the dry channel while increasing the width of the wet channel appears advantageous. In the wet channel, the increase in available CSA leads to a reduction in mean flow velocity, which in turn promotes enhanced evaporation, as evidenced by the figures.

Therefore, while evaporation appears to be enhanced, an open question remains regarding what would occur in a strongly turbulent regime (such as that promoted by TPMS structures) if the conductive thermal resistance bottleneck were removed, for instance by moving toward metallic HMX manufacturing. In that case, the larger heat flux transferred from the dry to the wet channel would increase the wall temperature raising the local saturation vapor pressure and effectively shifting the saturation limit upward and potentially reducing the achievable outlet relative humidity for a given wet channel length.

Despite the high outlet relative humidity levels observed in the wet channel, the wet-bulb effectiveness reported in Fig. 10a,b remains

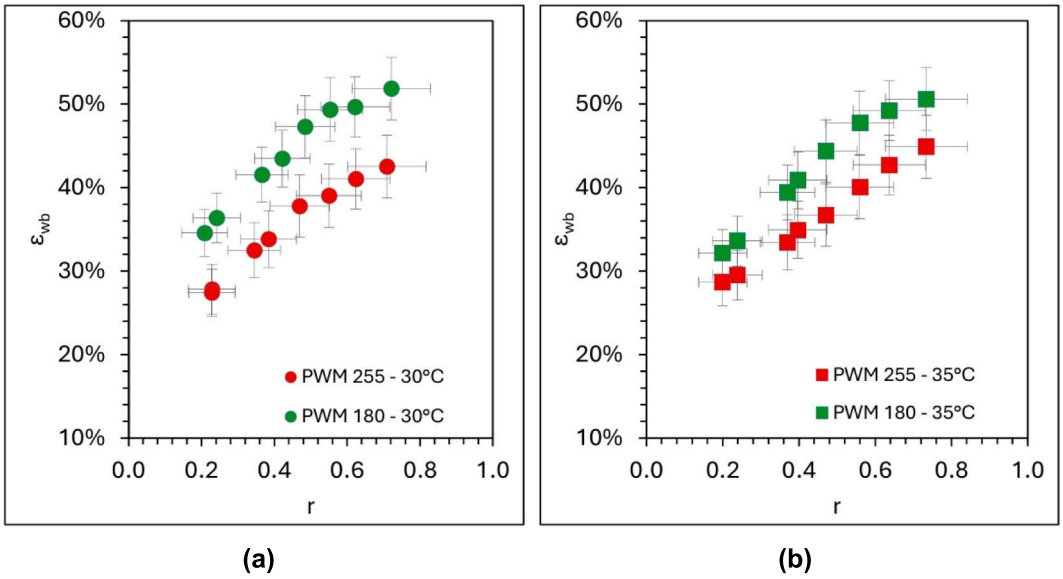

Fig. 10. Wet-bulb effectiveness ε_{wb} as a function of the recirculation ratio *r*at an inlet air temperature of 30 °C **(a)** and 35 °C **(b)** for two fan duty cycles (PWM 180 and PWM 255).

relatively low, reaching values slightly higher than 50% at the highest recirculation ratios (i.e. where higher ΔT are observed). For comparison, reference wet-bulb effectiveness values reported in the literature for dew point evaporative coolers are generally in the range of 90–130%.

This confirms that, although the working air stream approaches saturation, the system is still operating far from its full potential due to several factors such as: the limited length of the HMX and, in particular, the limited length of the dry channel; the high conductive thermal resistance of the heat transfer surface which, in high turbulent regimes, is the bottleneck; the poor wettability of the as-printed PLA surface.

Higher values are consistently obtained at the lower fan speed (PWM 180), where lower temperatures at the dry channel outlet are obtained, as reported in the previous paragraphs. The comparison between the figures also shows that the overall trends are preserved when the inlet temperature is increased to 35 °C, with values becoming closer to each other, partly due to the reduced variation in $T_{dry,out}$ at different velocity.

Due to the relatively small size of the tested prototype, a brief consideration on scaling effects is required: the current HMX dimensions (100 mm length) represent a proof-of-concept scale and it is important to note that M-cycle performance is strongly dependent on this. While extending the dry channel would increase the wet-bulb effectiveness by allowing the product air to approach the dew-point temperature more closely [15], it would also introduce a trade-off: since the temperature drop tends to flatten as it nears the dew-point, the volumetric cooling capacity is expected to decrease in longer configurations.

From an engineering perspective, the TPMS architecture facilitates modular scaling and enables the exploration of both parallel and series configurations; however, given the long 3D printing times, such analyses are more effectively performed numerically. Future investigations should therefore focus on the development and calibration of CFD models specifically tailored to gyroid-based HMXs, enabling comprehensive computational parametric analyses and extending the range of operating conditions and design variables beyond those experimentally accessible in the present study.

3.3. *Assessment of water distribution*

The test rig is equipped with a polyethylene film (thickness 0.2 mm) window, allowing thermographic investigation of the product air outlet from the HMX during operation (Fig. 11a), as the observed temperature distribution provides an indirect indication of how water is distributed within the HMX.

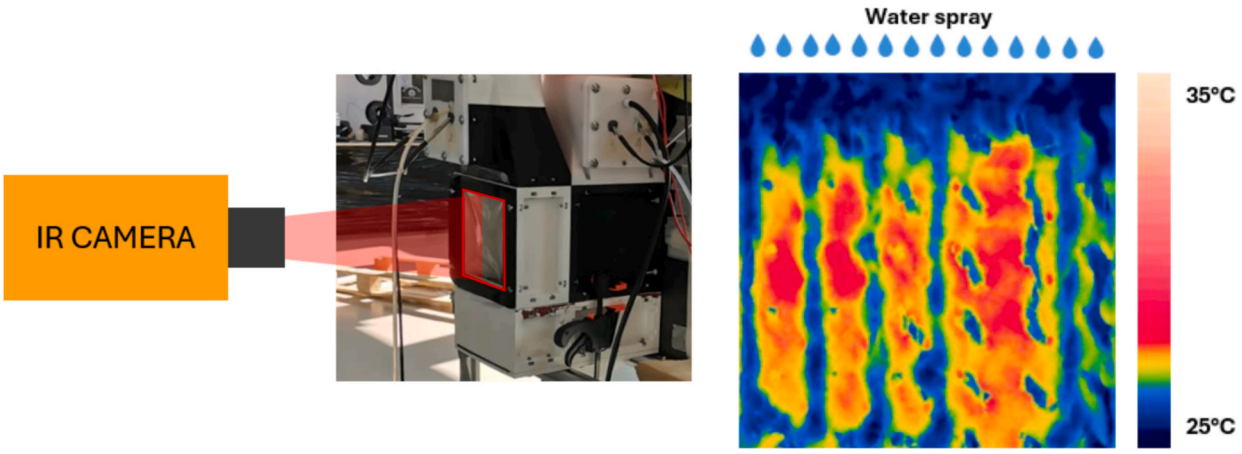

Fig. 11. **(a)** Infrared setup and **(b)** thermography of the gyroid HMX dry outlet during operation at 35 °C and PWM 180, showing temperature distribution across dry and wet channels and highlighting non-uniform wetting patterns.

Fig. 11b shows an IR image captured with a Flir T640 camera at the outlet of the product channel during one of the experimental runs, where the central region of the image exhibits localized hotspots, corresponding to the warmer air flowing through the dry channel. Conversely, colder regions indicate the presence of water films or droplets on the wet-channel surfaces. The uppermost portion appears consistently cold and without hotspots, suggesting a higher local water concentration, an observation consistent with the top-mounted spray configuration. Similarly, the rightmost portion of the heat and mass exchanger shows absence of hotspots.

The asymmetry observed in the central hotspot likely indicates non-uniform wetting within the wet channel, that may stem from both the complex internal geometry of the gyroid structure and the distribution pattern of the spray nozzles. This issue was also observed in the authors' previous work [24] and was attributed to hydraulic diameters below 8.5 mm. In the present case, where the hydraulic diameter exceeds this threshold, the maldistribution is more likely associated with the conical shape of the spray, which does not optimally match the cubic geometry of the tested HMX. This highlights the importance of future studies focusing on the influence of spray characteristics on water distribution and overall system performance, together with the study of surface coatings of the wet channel heat and mass transfer surface which may prove beneficial.

4. Conclusions

This work experimentally investigated the performance of a polymeric gyroid-based TPMS heat and mass exchanger operated as a dew point evaporative cooler. The results highlight both the strong potential and the current limitations associated with this unconventional geometry and fabrication process.

The fluid dynamic characterization of the gyroid-based HMX shows that the Fanning friction factor stabilizes at approximately 1 in the dry channel and around 1.2 in the wet channel for $Re > 700$, indicating the establishment of a fully turbulent flow regime. This transition occurs significantly earlier than in conventional HMX geometries and is directly attributable to the gyroid structure, whose continuous split-and-merge flow behavior effectively disrupts boundary layers even at relatively low air velocities.

From a thermodynamic perspective, the device was tested at two inlet air temperatures (30 °C and 35 °C), corresponding to relative humidity levels of 43% and 32%, respectively, with dry-channel air velocities ranging from 2.3 to 4.1 m/s and recirculation rates between 0.2 and 0.7. The HMX achieved a maximum temperature drop of 6.1 °C at an inlet temperature of 35 °C and peak of specific cooling capacities of 55.6 kW/m^3 at 35 °C and 39.4 kW/m^3 at 30 °C, exceeding the values typically reported in the literature for standard HMX geometries, while the COP peaked at 9.1. As the air velocity increases toward 4 m/s, the COP rapidly decreases, especially if compared to conventional cross-flow heat exchangers where, such velocities, still generate a laminar flow and higher COP values. This behavior indicates that gyroid-based devices should be operated at significantly lower characteristic velocities than those tested in this work and future investigations should therefore explore flow regimes approaching laminar conditions ($Re < 150$).

The psychrometric analysis of the wet channel showed that the gyroid structure consistently sustained strong evaporation, although the wet-bulb effectiveness peaked only slightly above 50%, partly limited by both the high conductive thermal resistance of the PLA, and the limited dimensions of the HMX. On the other hand, the outlet relative humidity in the wet channel remained above 83% across all tested operating conditions, confirming the effectiveness of the TPMS geometry in promoting mass transfer even on untreated PLA surfaces.

The combined analysis of relative humidity, wet-bulb effectiveness, and cooling capacity indicates that, for the HMX adopted in this study, the dry channel appears to be undersized and the cubic geometry is not optimal; under the tested conditions, extending the dry channel length would likely be more beneficial than further increasing the wet channel. In this context, numerical modelling could provide valuable insight by enabling the simulation of asymmetric channels in metallic TPMS structures, thereby supporting the development of pre-optimized HMX designs prior to subsequent experimental fabrication and testing.

Declaration of competing interest

The authors declare that they have no known competing financial interests or personal relationships that could have appeared to influence the work reported in this paper.

Acknowledgements

This project was funded under the National Recovery and Resilience Plan (NRRP), Mission 4 Component 2 Investment 1.5 Call for tender No. 3277 of 30/12/2021 of the Italian Ministry of University and Research funded by the European Union NextGenerationEU. Project code ECS00000033, Concession Decree No. 1052 of 23/06/2022 adopted by the Italian Ministry of University and Research, No. CUP D93C22000460001, “Ecosystem for Sustainable Transition in Emilia-Romagna” (Ecosister), Spoke 4.

N.M. also acknowledges the financial support of the FAR Dipartimentale 2025 program of the Dept. of Engineering ‘Enzo Ferrari’ - UniMORE for part of the instruments used in this study.

During the preparation of this work, the authors used Microsoft Copilot to improve the fluency and clarity of the English language. After using this tool, the authors reviewed and edited the content as needed and take full responsibility for the content of the publication.

Data availability

Data will be made available on request.

References

[1] H. Sadighi Dizaji, E.J. Hu, L. Chen, A comprehensive review of the maisotsenko-cycle based air conditioning systems, Energy 156 (2018) 725–749. Aug, https://doi.org/10.1016/j.energy.2018.05.086.

[2] F. Alsouda, N.S. Bennett, S.C. Saha, F. Salehi, M.S. Islam, Vapor compression cycle: a state-of-the-art review on cycle improvements, water and other natural refrigerants, Clean Technol. 5 (2) (2023) 584–608. May 2023, https://doi.org/10.3390/CLEANTECHNOL5020030.

[3] N. Kapilan, A.M. Isloor, S. Karinka, A Comprehensive Review on Evaporative Cooling Systems, Jun. 01, Elsevier B.V, 2023, https://doi.org/10.1016/j.rineng.2023.101059.

[4] M. Ali, W. Ahmad, N.A. Sheikh, H. Ali, R. Kousar, T. ur Rashid, Performance enhancement of a cross flow dew point indirect evaporative cooler with circular finned channel geometry, J. Build. Eng. 35 (2021) 101980, https://doi.org/10.1016/j.jobe.2020.101980.

[5] Z. Duan, Investigation of a Novel Dew Point Indirect Evaporative Air Conditioning System for Buildings, 2011.

[6] M.S. Alam, et al., A technological review of dew point evaporative cooling: experimental, analytical, numerical and optimization perspectives, J. Build. Eng. 91 (2024) 109544, https://doi.org/10.1016/j.jobe.2024.109544.

[7] J. Chu, W. Xu, Y. Fu, H. Huo, Experimental research on the cooling performance of a new regenerative dew point indirect evaporative cooler, J. Build. Eng. 43 (2021), https://doi.org/10.1016/j.jobe.2021.102921.

[8] Z. Duan, X. Zhao, J. Li, Design, fabrication and performance evaluation of a compact regenerative evaporative cooler: towards low energy cooling for buildings, Energy 140 (2017) 506–519, https://doi.org/10.1016/j.energy.2017.08.110.

[9] S. Kashyap, J. Sarkar, A. Kumar, Development and experimental analysis of a novel dual-mode counter-flow evaporative cooling device, Build. Environ. 205 (2021), https://doi.org/10.1016/j.buildenv.2021.108176.

[10] S. De Antonellis, L. Cignatta, C. Facchini, P. Liberati, Effect of heat exchanger plates geometry on performance of an indirect evaporative cooling system, Appl. Therm. Eng. 173 (2020), https://doi.org/10.1016/j.applthermaleng.2020.115200.

[11] V. Maisotsenko, “SU979796A1 - Unit for indirect evaporation cooling of air - Google Patents.” 2025 Accessed: Jul. 18, 2025. [Online]. Available: https://patents.google.com/patent/SU979796A1/en?oq=SU979796.

[12] C. Zhan, X. Zhao, S. Smith, S.B. Riffat, Numerical study of a m-cycle cross-flow heat exchanger for indirect evaporative cooling, Build. Environ. 46 (3) (2011) 657–668. Mar, https://doi.org/10.1016/j.buildenv.2010.09.011.

[13] Coolerado - Seeley International, Accessed: Jul. 20, 2025. [Online]. Available: https://www.seeleyinternational.com/us/commercial/brands/coolerado/, 2025.
[14] M.H. Mahmood, M. Sultan, T. Miyazaki, S. Koyama, V.S. Maisotsenko, Overview of the maisotsenko cycle – a way towards dew point evaporative cooling, Renew. Sust. Energ. Rev. 66 (2016) 537–555. Dec, https://doi.org/10.1016/J.RSER.2016.08.022.
[15] M. Jradi, S. Riffat, Experimental and numerical investigation of a dew-point cooling system for thermal comfort in buildings, Appl. Energy 132 (2014) 524–535. Nov, https://doi.org/10.1016/J.APENERGY.2014.07.040.
[16] D. Pandelidis, S. Anisimov, W.M. Worek, Performance study of the maisotsenko cycle heat exchangers in different air-conditioning applications, Int. J. Heat Mass Transf. 81 (2015) 207–221. Feb, https://doi.org/10.1016/J.IJHEATMASSTRANSFER.2014.10.033.
[17] S. Rasheed, M. Ali, H. Ali, N.A. Sheikh, G. Li, Design evolution of indirect evaporative air-cooling system through multiple configurations for the enhancement of heat and mass transfer mechanism, Int. Commun. Heat Mass Transf. 160 (2025), https://doi.org/10.1016/j.icheatmasstransfer.2024.108393. Jan.
[18] S. Nardini, B. Buonomo, K. Dutkowski, M. Kruzel, K. Rokosz, Review of the state-of-the-art uses of minimal surfaces in heat transfer, Energies (2022), https://doi.org/10.3390/en15217994.
[19] B.W. Reynolds, C.J. Fee, K.R. Morison, D.J. Holland, Characterisation of heat transfer within 3D printed TPMS heat exchangers, Int. J. Heat Mass Transf. 212 (2023), https://doi.org/10.1016/j.ijheatmasstransfer.2023.124264. Sep.
[20] J. Iyer, T. Moore, D. Nguyen, P. Roy, J. Stolaroff, Heat transfer and pressure drop characteristics of heat exchangers based on triply periodic minimal and periodic nodal surfaces, Appl. Therm. Eng. 209 (2022), https://doi.org/10.1016/j.applthermaleng.2022.118192. Jun.
[21] T. Dixit, E. Al-Hajri, M.C. Paul, P. Nithiarasu, S. Kumar, High performance, microarchitected, compact heat exchanger enabled by 3D printing, Appl. Therm. Eng. 210 (2022), https://doi.org/10.1016/j.applthermaleng.2022.118339. Jun.
[22] K. Yan, J. Wang, L. Li, H. Deng, Numerical investigation into thermo-hydraulic characteristics and mixing performance of triply periodic minimal surface-structured heat exchangers, Appl. Therm. Eng. 230 (2023), https://doi.org/10.1016/j.applthermaleng.2023.120748. Jul.
[23] A.H. Schoen, Infinite Periodic Minimal Surfaces without Self-Intersections, May, 1970.
[24] N. Morselli, et al., An experimental investigation of indirect evaporative cooling in gyroid-based heat exchangers, Appl. Therm. Eng. 275 (2025) 126808. Sep, https://doi.org/10.1016/J.APPLTHERMALENG.2025.126808.
[25] O. Al-Ketan, R.K. Abu Al-Rub, MSLattice: a free software for generating uniform and graded lattices based on triply periodic minimal surfaces, Mater. Des. Process. Commun. 3 (6) (2021) e205. Dec, https://doi.org/10.1002/mdp2.205.
[26] D.A. Reay, P.A. Kew, R.J. McGlen, Heat transfer and fluid flow theory, Heat Pipes (2014) 15–64. Jan, https://doi.org/10.1016/B978-0-08-098266-3.00002-9.
[27] F.P. Incropera, D.P. DeWitt, Fundamentals of Heat and Mass Transfer, 4th edition, John Wiley & Sons, Inc., New York City, New York, 1996.
[28] K. Yan, H. Deng, Y. Xiao, J. Wang, Y. Luo, J. Yan, Influence of polishing process on surface morphology and thermo-hydraulic performance of additively manufactured gyroid-structured heat exchanger, Appl. Therm. Eng. 253 (2024) 123828. Sep, https://doi.org/10.1016/J.APPLTHERMALENG.2024.123828.
[29] A.M.S.J. Kline, The description of uncertainties in a single sample experiments, Mech. Eng. 75 (1953) 3–8.
[30] K. Yan, H. Deng, Y. Wu, J. Wang, Y. Huang, Effects of lattice geometric manipulation on thermo-hydraulic performance of gyroid-structured heat exchanger: a numerical study, Int. J. Heat Mass Transf. 248 (2025) 127217. Sep, https://doi.org/10.1016/J.IJHEATMASSTRANSFER.2025.127217.
[31] Z. Duan, C. Zhan, X. Zhao, X. Dong, Experimental study of a counter-flow regenerative evaporative cooler, Build. Environ. 104 (2016) 47–58. Aug, https://doi.org/10.1016/j.buildenv.2016.04.029.
[32] D. Pandelidis, S. Anisimov, Numerical analysis of the heat and mass transfer processes in selected M-cycle heat exchangers for the dew point evaporative cooling, Energy Convers. Manag. 90 (2015) 62–83. Jan, https://doi.org/10.1016/J.ENCONMAN.2014.11.008.
[33] S. De Antonellis, C.M. Joppolo, P. Liberati, S. Milani, L. Molinaroli, Experimental analysis of a cross flow indirect evaporative cooling system, Energ. Buildings 121 (2016) 130–138. Jun, https://doi.org/10.1016/j.enbuild.2016.03.076.